Journal of
Synchrotron Radiation

ISSN 0909-0495

Received 2 March 2012
Accepted 10 May 2012

Synchrotron microanalysis techniques applied to potential photovoltaic materials

Julie Villanova,* Jaime Segura-Ruiz, Tamzin Lafford and Gema Martinez-Criado

ESRF, 6 rue Jules Horowitz, BP 220, 38043 Grenoble, France. E-mail: julie.villanova@esrf.fr

X-ray synchrotron radiation techniques are used to characterize photovoltaic-related semiconductors. Micro-X-ray-fluorescence and X-ray beam induced current mapping of multicrystalline silicon photovoltaic cells show metallic impurities accumulating at the interface of crystallographic defects, and current variations over the cell that are attributed to bulk defects and structural variation of the silicon. Similarly, studies on a single-crystal GaAs using X-ray fluorescence and X-ray excited optical luminescence show an inhomogeneous As distribution correlated with the photoluminescence signal, with higher As concentration regions having stronger photoluminescence signal. Both examples show how the combination of synchrotron microanalysis techniques can contribute to a better understanding of the optical properties of photovoltaic materials.

Keywords: microanalysis; photovoltaic; XRF; XBIC; XEOL.

1. Introduction

Efficient dedicated characterization tools are essential for developing advanced materials for solar cells. Compared with standard and well established laboratory tools, synchrotron radiation techniques can unravel structure–property relationships thanks to the large penetration depths, high throughput and superior tunability in terms of probe (energy, spot size, photon flux, polarization, *etc.*). The current levels of hard X-ray beam intensities and *in situ* capabilities allow parallel signal acquisition and analysis of buried structures and phenomena, under realistic operation conditions. Indeed, synchrotron-radiation-based methods have been proven as major sources of information on solar cells. X-ray diffraction (XRD) and small-angle X-ray scattering techniques have provided structural information at the atomic and at the mesoscopic scales (Schorr, 2011; Chiu *et al.*, 2008). X-ray absorption spectroscopy (XAS) has delivered information on local phenomena helping to identify degradation and failure mechanisms (Buonassisi *et al.*, 2005*a*). Insight into chemical states and bonding has become accessible *via* X-ray spectroscopy techniques (Lauermann *et al.*, 2005). However, to facilitate further breakthroughs, new methodological improvements are necessary in this field; for instance, coupling advanced X-ray characterization tools; higher-resolution imaging techniques with multiple length domains to correlate data acquired at different scales; and the complementarity of combining techniques. In this respect, the characterization of photovoltaic materials at the hard X-ray microprobe ID22 at the European Synchrotron Radiation Facility (ESRF) has recently stimulated the application of X-ray fluorescence (XRF), X-ray beam induced current (XBIC) and X-ray excited optical luminescence (XEOL) at the micrometre scales. Several photovoltaic-related issues have been addressed at ID22; for example, the formation of impurity aggregates, radiative recombination centers, and breakdown effects (Trushin *et al.*, 2010; Gundel *et al.*, 2009, 2010). Furthermore, the increased spatial resolution towards nanoscales in two-dimensional imaging techniques reaches a previously inaccessible level of detail (Kwapil *et al.*, 2009). In this work we report a few recent examples of these hard X-ray microanalytical tools applied to two photovoltaic-related semiconductors: Si and GaAs.

2. Experimental details

The synchrotron-radiation-based measurements were performed at the hard X-ray microprobe beamline ID22 at the ESRF. The high-β straight section of ID22 is equipped with two insertion devices, an in-vacuum U23 and a revolver U35/U19. The optical layout of the beamline consists of several pairs of slits, attenuators, a horizontally deflecting Si mirror, and a double Si crystal monochromator that is moveable so that either pink beam or monochromatic beam mode can be operated in the experimental hutches. There are two experimental stations that share common instrumental equipment shown in Fig. 1: an X-ray focusing device (Kirkpatrick–Baez mirrors), a high-precision piezostage to align and to raster-scan the sample in the beam, a visible-light microscope (VLM) to visualize the regions of interest of the samples, as well as various detection schemes and two-dimensional/three-dimensional X-ray imaging (XRI) detectors. The two experimental hutches are clearly identified by their spatial resolu-

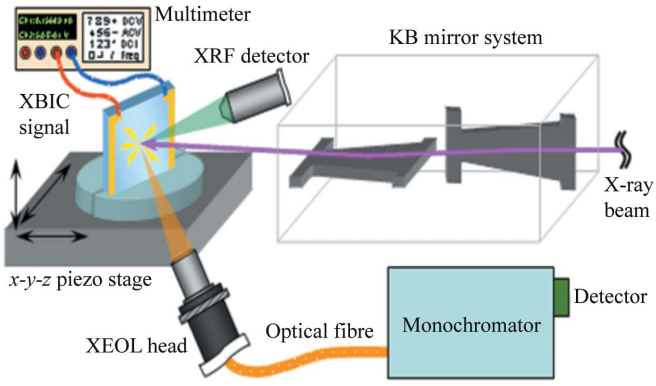

Figure 1
Experimental configuration for XEOL and XBIC measurements located at the ID22 beamline at the ESRF.

tions: EH1 devoted to microanalysis and EH2, also known as the ID22 nano-imaging station (ID22NI), exclusively used for nanoanalysis. Both hutches are commonly dedicated to hard X-ray microanalysis consisting of the combination of XRF, XAS, XRD and XRI techniques in the multi-keV X-ray regime (Martinez-Criado *et al.*, 2012). In addition, in order to perform even more challenging experiments mainly driven by semiconductor research, and to enlarge the experimental capabilities of the beamline in the microspectroscopy domain, micro-XBIC and micro-XEOL methods have also recently been integrated within the multimodal detection approaches as displayed in Fig. 1 (Martinez-Criado *et al.*, 2011; Trushin *et al.*, 2010). In general, XEOL and XBIC are complementary tools used to discriminate areas of semiconductors according to their electrical behaviour and/or recombination activity. Another advantage of both techniques in comparison with standard photoluminescence and light beam induced current (LBIC) measurements is the long absorption length of the X-ray excitation, which allows measurements of buried layers without being influenced by surface effects. Silicon drift detectors or a 13-element Si(Li) detector are routinely available to detect XRF on the microprobe, whereas Keithley 6485 picoamperemeters are commonly used to register XBIC signals. The XEOL arrangements are basically preconfigured modules optimized for three different wavelength ranges: (i) 360–800 nm, (ii) 800–1600 nm, (iii) 1600–2200 nm. Each module comprises motorized optics to collect and focus the XEOL signal on an optical fibre that transmits the light to a spectrometer. The monochromator separates the light into its different wavelengths which are then incident on a linear charge-coupled-device detector. This combination produces fast acquisitions and provides high spectral resolution and maximum efficiency over the entire optical wavelength range (Martinez-Criado *et al.*, 2006).

3. XBIC

Fig. 2 displays the scanning electron microscopy (SEM) image (*a*), µ-XRF (*b* and *c*) and µ-XBIC (*d*) measurements collected on a multicrystalline silicon photovoltaic cell in the region of a

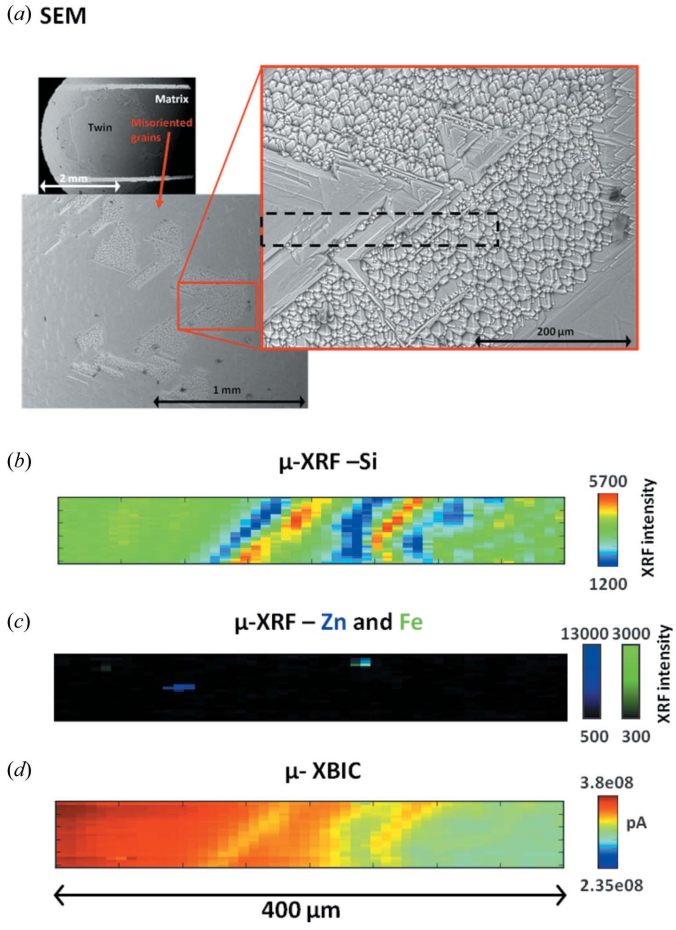

Figure 2
SEM image of the surface of a Si photovoltaic cell (*a*). XRF intensity map of Si (*b*), and Zn and Fe (*c*), acquired over the region delimited by the black box in the higher-resolution SEM image. XBIC map acquired simultaneously with the XRF (*d*). All measurements were carried out at room temperature.

crystalline defect consisting of a twin and misoriented grains within the bulk matrix. The µ-XRF and µ-XBIC maps were acquired in the experimental hutch EH1 with a micrometre-sized beam [8 µm × 2 µm (H × V)] over a sample area of 400 µm × 32 µm (H × V) with an excitation energy of 17 keV. The XRF maps were recorded by measuring the different fluorescence line intensities at an incident angle of 45 ± 5° with respect to the sample surface. The step size was 8 µm × 2 µm (H × V) to match the beam size, and integration times were determined by the counting statistics (∼8 s point^{-1}). The information depth of the fluorescence photons is element dependent and is about 9 µm for Si, 26 µm for Fe and 61 µm for Zn at 17 keV. The measurement sensitivity is around 0.2 ± 0.1 p.p.m. for the metallic impurities.

The SEM image (Fig. 2*a*) shows that the scanned area is characterized by morphological and crystalline differences within the Si matrix. The Si matrix is (111)-oriented, and both the twin and the other grains exhibit small, predominantly pyramid-shaped, surface pits. These features arise from a texturization step in the cell processing, designed to reduce optical reflectivity and enhance optical confinement, and thus

to increase the efficiency of the solar cell. The shape of the grain boundary correlates with variations observed in the μ-XRF maps. The uniform green part on the left of the XRF map (Fig. 2*b*) corresponds to the twin, whereas the spatial fluctuations observed near the centre (red and blue stripes) correspond very well to the boundaries between twin and misoriented grains. Thus, our observations reveal the sensitivity of the μ-XRF method to the morphological and structural order present on and near the silicon surface.

Some micrometric aggregates of iron and zinc, that are not surface contamination, were also found at the grain boundaries, as illustrated in Fig. 2(*c*). Such impurities, very often localized at the grain boundaries (Buonassisi *et al.*, 2006*a*,*b*), do not generally have a significant impact on the photovoltaic performance of the cell.

The μ-XBIC measurements clearly correlate with the XRF map of the silicon with respect to the interface region between the twin and the misoriented grains [compare Figs. 2(*b*) and 2(*d*)]. While a photocurrent variation of about 20% can be deduced between the two areas, the change in the Si only corresponds to ∼2%. This substantial difference could result from the bulk sensitivity of the μ-XBIC method (determined by the penetration depth; here equal to the thickness of the sample). The μ-XBIC signal is not only linked to the textured surface, but also to the dispersed small metallic nanoprecipitates with a concentration of $\sim 10^{12}\,\mathrm{cm}^{-3}$ (metallurgical silicon), or to the high dislocation density (El Ghitani *et al.*, 1993). The dimensions of nanoclusters are below the spatial resolution reached in experimental hutch EH1 but are detectable in experimental hutch EH2 which is optimized for a 100 nm beam size (Buonassisi *et al.*, 2005*b*). In summary, the combination of μ-XRF and μ-XBIC measurements permits a direct correlation between chemical and photocurrent changes within the sample matrix. In comparison with LBIC, where the carriers are photo-generated within a few tens of micrometres of the surface and then diffuse through the bulk, the X-ray beam passes through the total thickness of the sample, generating carriers along the full length of its path.

4. XEOL

Fig. 3(*a*) shows the average XRF spectrum of a single-crystal GaAs compound semiconductor sample, with a thickness of 300 μm, acquired over an area of 140 μm × 100 μm in experimental hutch EH1. The XRF as well as XEOL signals were simultaneously excited with a 12.2 keV monochromatic beam focused to a spot size of 3.3 μm × 1.2 μm (H × V). For this energy the information depths for Ga and As fluorescence and for XEOL photons are 6.5 μm, 4.8 μm and 0.5 μm, respectively. The sample area was scanned with a step size of 4 μm in both vertical and horizontal directions, and a counting time of 2 s point^{-1}. The X-ray characteristic lines of the major elements (Ga and As) and minor dopants (unintentional Ni and Fe) are indicated. Setting regions of interest around the fluorescence lines of each element, Figs. 3(*c*)–3(*f*) display the respective intensity maps. In comparison, Fig. 3(*b*) shows the XEOL intensity map of the luminescence peak located at

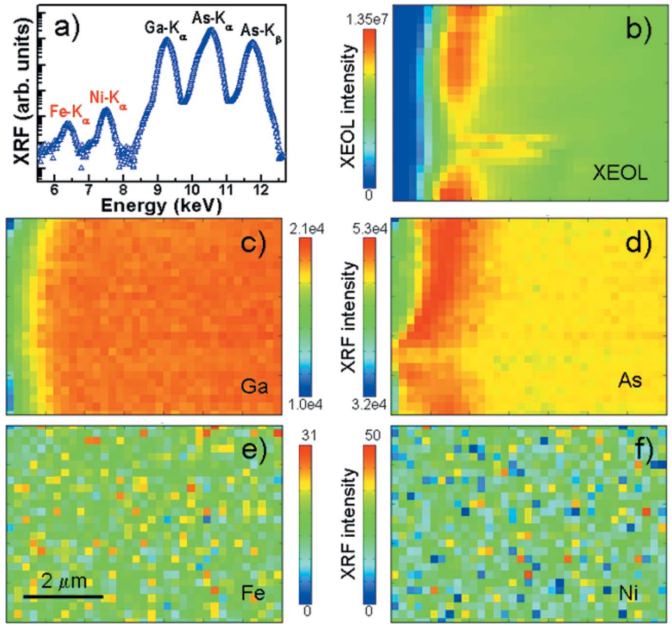

Figure 3
Average XRF spectrum acquired over a 140 μm × 100 μm area of a GaAs sample (*a*). XEOL intensity map of the peak centred around 1.50 eV and associated with a bound-exciton transition (*b*). XRF intensity maps over the scanned area of Ga (*c*), As (*d*), Fe (*e*) and Ni (*f*) *Kα* lines. XEOL and XRF maps were acquired simultaneously and at liquid-nitrogen temperature.

∼1.5 eV, which is associated with the recombination of a donor bound-exciton (D^0X) (Sell *et al.*, 1973). The edge of the sample can be easily identified on the left. The XEOL signal falls to zero in this region but not the fluorescence, probably due to an irregular sample cut, reflecting the smaller information depth of the XEOL compared with XRF photons. The Ga fluorescence map exhibits an almost constant intensity beyond the edge, suggesting a homogeneous distribution all over the scanned area. However, the As fluorescence map shows regions with higher intensity close to the edge, and an invariable distribution over the right half. Regions having a higher XRF intensity suggest a deviation from exact 1:1 GaAs stoichiometry. This deviation could be due to arsenic-related bulk defects, like arsenic antisites and interstitials (Chadi & Chang, 1989; Stellmacher *et al.*, 2001), or arsenic precipitates (McInturff *et al.*, 1992; Feenstra *et al.*, 1993), known to be recombination centres (Viturro *et al.*, 1992). The XEOL map shows areas with a stronger XEOL signal, indicating a higher density of donors or their transition rates. There seems to be a correlation between high XEOL signals and As fluorescence intensities. The former would suggest that the D^0X recombination could be associated with As-related defects. However, more detailed investigations are necessary to complete the picture of the statistical dependence between the two data sets. Finally, the XRF maps of both Ni and Fe exhibit a random distribution, without any correlation with the XEOL map. Transition metals are efficient optically active recombination centres in GaAs, as observed in the photoluminescence of doped samples (Van de Ven *et al.*, 1986). However, the absence of any observable dependent phenomena between

the XEOL and the Ni/Fe maps points out that these elements are not involved in the D^0X recombination, *i.e.* neither the Ni nor the Fe impurities act as donor centres. This is a good example of how the combination of μ-XEOL and μ-XRF imaging helps to shed more light on the effect of dopants and defects on the optical properties of photovoltaic cells.

5. Conclusion

In summary, synchrotron microanalytical techniques were applied to two potential photovoltaic-related semiconductors: multicrystalline Si and single-crystal GaAs. μ-XRF and μ-XBIC measurements on a Si photovoltaic cell showed micrometre-sized aggregates of metallic impurities at the interface between crystallographic defects, whereas changes in the X-ray beam induced current were attributed to structural modifications and bulk defects. Thus, the combination of both tools provides critical information for promoting improvements in the performance of solar cells. In another example, using μ-XRF and μ-XEOL, a heterogeneous distribution of As in GaAs accompanied by striking luminescence changes was observed. Although more detailed investigations are required to explain this finding, our observations show a direct path to a comprehensive understanding of the relationship between material, structural and optical properties in photovoltaic cells.

We thank D. Camel and S. Dubois from CEA/INES for supplying the mc-Si sample and for interesting discussions about solar cells.

References

Buonassisi, T., Istratov, A. A., Heuer, M., Marcus, M. A., Jonczyk, R., Isenberg, J., Lai, B., Cai, Z., Heald, S., Warta, W., Schindler, R., Willeke, G. & Weber, E. R. (2005*b*). *J. Appl. Phys.* **97**, 074901.

Buonassisi, T., Istratov, A. A., Marcus, M. A., Lai, B., Cai, Z. H., Heald, S. M. & Weber, E. R. (2005*a*). *Nat. Mater.* **4**, 676–679.

Buonassisi, T., Istratov, A. A., Pickett, M. D., Heuer, M., Kalejs, J. P., Hahn, G., Marcus, M. A., Lai, B., Cai, Z., Heald, S. M., Ciszek, T. F., Clark, R. F., Cunningham, D. W., Gabor, A. M., Jonczyk, R., Narayanan, S., Sauar, E. & Weber, E. R. (2006*a*). *Prog. Photovolt. Res. Appl.* **14**, 513–531.

Buonassisi, T., Istratov, A. A., Pickett, M. D., Marcus, M. A., Ciszek, T. F. & Weber, E. R. (2006*b*). *Appl. Phy. Lett.* **89**, 042102.

Chadi, D. J. & Chang, K. J. (1989). *Phys. Rev. B*, **39**, 10063–10074.

Chiu, M. Y., Jeng, U. S., Su, C. H., Liang, K. S. & Wei, K. H. (2008). *Adv. Mater.* **20**, 2573–2578.

El Ghitani, H., Pasquinelli, M. & Martinuzzi, S. (1993). *J. Phys. III*, **3**, 1941–1946.

Feenstra, R. M., Woodall, J. M. & Pettit, G. D. (1993). *Phys. Rev. Lett.* **71**, 1176–1179.

Gundel, P., Martinez-Criado, G., Schubert, M. C., Sans, J. A., Kwapil, W., Warta, W. & Weber, E. R. (2009). *Phys. Status Solidi RRL*, **3**, 275–277.

Gundel, P., Schubert, M. C., Heinz, F. D., Kwapil, W., Warta, W., Martinez-Criado, G., Reiche, M. & Weber, E. R. (2010). *J. Appl. Phys.* **108**, 103707.

Kwapil, W., Gundel, P., Schubert, M. C., Heinz, F. D., Warta, W., Weber, E. R., Goetzberger, A. & Martinez-Criado, G. (2009). *Appl. Phys. Lett.* **95**, 232113.

Lauermann, L., Pistor, P., Kotschau, I. & Bar, M. (2005). *Mater. Res. Soc. Symp. Proc.* **865**, 41–52.

McInturff, D. T., Woodall, J. M., Warren, A. C., Braslau, N., Pettit, G. D., Kirchner, P. D. & Melloch, M. R. (1992). *Appl. Phys. Lett.* **60**, 448–450.

Martinez-Criado, G., Alen, B., Homs, A., Somogyi, A., Miskys, C., Susini, J., Pereira-Lachataignerais, J. & Martinez-Pastor, J. (2006). *Appl. Phys. Lett.* **89**, 221913.

Martinez-Criado, G., Alén, B., Sans, J. A., Homs, A., Kieffer, I., Tucoulou, R., Cloetens, P., Segura-Ruiz, J., Susini, J., Yoo, J. & Yi, G. (2011). *Nucl. Instrum. Methods Phys. Res. B*, doi:10.1016/j.nimb.2011.08.013.

Martinez-Criado, G., Tucoulou, R., Cloetens, P., Bleuet, P., Bohic, S., Cauzid, J., Kieffer, I., Kosior, E., Labouré, S., Petitgirard, S., Rack, A., Sans, J. A., Segura-Ruiz, J., Suhonen, H., Susini, J. & Villanova, J. (2012). *J. Synchrotron Rad.* **19**, 10–18.

Schorr, S. (2011). *Solar Energy Mater. Solar Cells*, **95**, 1482–1488.

Sell, D. D., Stokowski, S. E., Dingle, R. & DiLorenzo, J. V. (1973). *Phys. Rev. B*, **7**, 4568–4586.

Stellmacher, M., Bisaro, R., Galtier, P., Nagle, J., Khirouni, K. & Bourgoin, J. C. (2001). *Semicond. Sci. Technol.* **16**, 440–446.

Trushin, M., Seifert, W., Vyvenko, O., Bauer, J., Martinez-Criado, G., Salome, M. & Kittler, M. (2010). *Nucl. Instrum. Methods Phys. Res. B*, **268**, 254–258.

Van de Ven, J., Hartmann, W. J. A. M. & Giling, L. J. (1986). *J. Appl. Phys.* **60**, 3735.

Viturro, R. E., Melloch, M. R. & Woodall, J. M. (1992). *Appl. Phys. Lett.* **60**, 3007.